CrossMark

Measuring the D/H Ratios of Exoplanets and Brown Dwarfs

Caroline V. Morley[1] , Andrew J. Skemer[2] , Brittany E. Miles[2] , Michael R. Line[3] , Eric D. Lopez[4], Matteo Brogi[5,6,7] ,
Richard S. Freedman[8,9], and Mark S. Marley[9]

[1] Department of Astronomy, University of Texas at Austin, Austin, TX, USA
[2] Department of Astronomy & Astrophysics, University of California Santa Cruz, Santa Cruz, CA, USA
[3] Arizona State University, Tempe, AZ, USA
[4] NASA Goddard Space Flight Center, Greenbelt, MD, USA
[5] Department of Physics, University of Warwick, Coventry CV4 7AL, UK
[6] INAF—Osservatorio Astrofisico di Torino, Via Osservatorio 20, I-10025, Pino Torinese, Italy
[7] Centre for Exoplanets and Habitability, University of Warwick, Gibbet Hill Road, Coventry CV4 7AL, UK
[8] SETI Institute, Mountain View, CA, USA
[9] NASA Ames Research Center, Mountain View, CA, USA

Abstract

The relative abundance of deuterium and hydrogen is a potent tracer of planet formation and evolution. Jupiter and Saturn have protosolar atmospheric D/H ratios, a relic of substantial gas accretion from the nebula, while the atmospheres of Neptune and Uranus are enhanced in D by accretion of ices into their envelopes. For terrestrial planets, D/H ratios are used to determine the mechanisms of volatile delivery and subsequent atmosphere loss over the lifetime of the planet. Planets and brown dwarfs more massive than $\sim$13 M_J quickly fuse their initial D reservoir. Here, we simulate spectra for giant exoplanets and brown dwarfs (2 $M_{Neptune}$ to $\sim$10 $M_{Jupiter}$) from $T_{eff} = 200$–1800 K including both CH_3D and HDO to determine the observability of these dominant deuterium isotopologues in mid-infrared thermal emission spectra. Colder objects have stronger molecular features in their spectra, due to the temperature dependence of molecular cross sections. CH_3D is easier to observe than HDO at all temperatures considered, due to the strength of its absorption bands and locations of features at wavelengths with few other strong absorption features. We predict that for nearby cool brown dwarfs, the CH_3D abundance can be measured at high signal to noise with the *James Webb Space Telescope* (*JWST*); for objects from 200 to 800 K closer than 10 pc, a protosolar D/H ratio would be readily observable in 2.5 hr. Moderately young Jupiter-mass planets (100–300 Myr) and young Neptunes (10 Myr) may be discovered with *JWST* and provide the best targets for detecting deuterium on an exoplanet in the coming decade. Future telescope designs should consider the importance of isotopes for understanding the formation and evolution of planetary atmospheres.

Key words: brown dwarfs – planets and satellites: atmospheres – planets and satellites: gaseous planets

1. Introduction

With current instruments, it is possible to detect molecules and elements in exoplanet and brown dwarf atmospheres (e.g., Charbonneau et al. 2002; Kirkpatrick 2005; Kreidberg et al. 2014). The atmospheric enrichment and ratios of elemental abundances inform us about how an object formed: the atmospheres of brown dwarfs that collapse directly out of a molecular cloud are predicted to form with the same elemental abundances as more massive stars forming in that cloud, while planets that form in a disk via core accretion and gas/planetesimal accretion will have abundance patterns that reflect the material available at their locations in the disk (Öberg et al. 2011). For example, planets that form beyond the water ice line will accrete both gas and water-rich ices into their atmospheres; depending on the ratio of gas to ice accreted, the object would have a supersolar or subsolar metallicity and C/O ratio (Espinoza et al. 2017).

In studies of the solar system, a complementary and critical tool for tracing planet formation and evolution is the relative abundances of different isotopes of the same element. One important element is deuterium: the deuterium to hydrogen (D/H) ratio traces a host of different physical processes in an atmosphere, including accretion of solids and gas, atmospheric escape, and deuterium fusion (Owen 1992; Lecluse et al. 1996). In this Letter, in Section 2 we will review these processes to provide motivation for the simulations, in Section 3 we

describe the model atmospheres, in Section 4 we examine the possibilities for detection of deuterium in an exoplanet atmosphere, and in Section 5 we discuss the implications of such a detection.

2. D/H Ratios in Planets and Brown Dwarfs

The D/H ratio can vary substantially from the galactic average; measurements for selected objects are shown in Figure 1. The primordial D/H ratio in the universe, set by Big Bang Nucleosynthesis, is $(2.8 \pm 0.2) \times 10^{-5}$ (Pettini et al. 2008). The Milky Way's D/H ratio in the gas of the interstellar medium varies along lines of sight by a factor of several, with a mean D/H ratio of $(2.0 \pm 0.1) \times 10^{-5}$, typically measured using absorption line spectroscopy of atomic H and D in the far-UV (Prodanović et al. 2010). Ices, both interstellar and within disks, become enhanced in deuterium through several chemical pathways at the cold temperatures ($<$50 K) present in these environments: gas-phase ion–neutral reactions and grain-surface formation from ionization-generated hydrogen and deuterium atoms from H_2 (Cleeves et al. 2014). D/H ratios in ices are typically measured at millimeter wavelengths using sublimating ice (either from comets or around protostars).
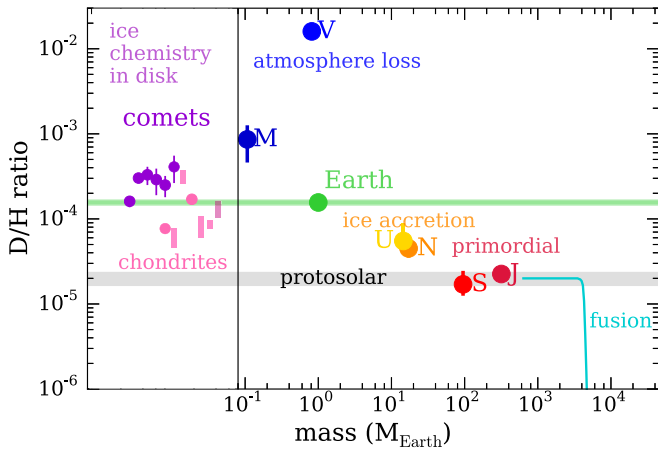
Figure 1. D/H ratio vs. mass of selected solar system objects. From left to right, selected comets, chondrites and lunar apatite (Hartogh et al. 2011; Cleeves et al. 2014), Mars, Venus, Earth (Drake 2005), Uranus, Neptune, Saturn, Jupiter (Hartogh et al. 2011), and model brown dwarfs (Spiegel et al. 2011) are shown. The protosolar and Earth D/H vs. ratio are shown as shaded bars. Points with error bars show single measurements; shaded bars show ranges over multiple measurements.

2.1. D/H in Giant Planets Traces Accretion of Solids

Deuterium was first detected outside of the Earth in Jupiter's atmosphere by Beer et al. (1972). Since then, the deuterium abundances in each of the giant planets' atmospheres have been measured in the near- and mid-infrared using CH_3D features and in the visible and far-infrared using HD rotational features (Knacke et al. 1982; Kunde et al. 1982; Courtin et al. 1984; de Bergh et al. 1986, 1990; Feuchtgruber et al. 1999; Lellouch et al. 2001, 2010). Jupiter and Saturn have D/H ratios consistent with the protosolar value, though, intriguingly, different from each other as measured using HD features with *Cassini* Composite Infrared Spectrometer: Jupiter's D/H is $(2.95 \pm 0.55) \times 10^{-5}$ and Saturn's is $(2.1 \pm 0.13) \times 10^{-5}$ (Pierel et al. 2017), with Saturn's lower abundance in conflict with predictions from models (Guillot 1999). Uranus's and Neptune's atmospheres are enhanced in deuterium by a factor of $\sim$2.5.

The classical picture is that the giant planets formed by accretion of ices and gases onto a core of $\sim$10–15 M_{Earth} (Stevenson 1982). For Jupiter and Saturn, the relative mass of the core and heavy elements is small compared to the gas accreted, so the D/H ratio is expected to trace the primordial composition of the solar nebula gas. For Uranus and Neptune, more than half of their total masses were accreted as ices; their envelopes are enhanced compared to the solar nebula gas, tracing the relative amount of D-enriched ices that accreted. Assuming that all ices are mainly water, the D/H ratio of the planet is

$$(D/H)_{planet} = (D/H)_{ices}(1 - x_{H_2}) + (D/H)_{proto}x_{H_2}, \quad (1)$$

where $(D/H)_{planet}$ is the D/H ratio in the planet, $(D/H)_{ices}$ is the D/H ratio in ices, $(D/H)_{proto}$ is the D/H ratio in the protosolar gas, and x_{H_2} is the volume mixing ratio of H_2 in the planet (Lecluse et al. 1996). Much of this ice is incorporated into planetary cores, but models predict that the interior ices exchange deuterium with the hydrogen reservoir (Guillot 1999).

2.2. D/H in Terrestrial Planets Traces Both Volatile Accretion and Atmosphere Loss

Earth, Mars, and Venus have distinct D/H ratios shaped by accretion of volatiles and subsequent atmospheric escape.

The D/H ratios of comets in the Oort Cloud are higher than that of the Earth, suggesting that Earth likely did not accrete the majority of its volatiles from comets (Drake & Righter 2002), but instead from chondrites. However, Hartogh et al. (2011) measured the D/H ratio in a Jupiter-family comet, finding an Earth-like D/H ratio and suggesting that comets and chrondrites may both have played a role in volatile delivery.

Venus's atmosphere is substantially enhanced in deuterium, by a factor of $\sim$100 above Earth's (Donahue & Pollack 1983). As Venus went through a runaway greenhouse, its oceans evaporated and H_2O photodissociated in its upper atmosphere. The lower mass of H caused it to be more easily lost than D (Donahue & Pollack 1983; Chamberlain & Hunten 1987).

Mars' D/H ratio is similar to Oort cloud comets. Since Mars does not have plate tectonics that recycle the crust with mantle material, this may reflect a late veneer of accretion from comets rather than a primordial reservoir (Drake 2005).

2.3. D/H in Brown Dwarfs Traces Deuterium Fusion

Brown dwarfs form with approximately protosolar abundances. Those more massive than 20 M_J will efficiently fuse almost all deuterium within 20 Myr; objects under 11 M_J will never fuse their deuterium, retaining primordial abundances (Saumon et al. 1996; Spiegel et al. 2011). The mass at which a brown dwarf will have burned 50% of its deuterium is roughly 13 M_J, but depends slightly on initial He fraction, metallicity, and primordial D/H ratio, and is expected to typically range between 12.2 and 13.7 M_J (Spiegel et al. 2011). Most D fusion occurs in the first 100–300 Myr.

3. Methods

3.1. Atmosphere Models

We model the impact of two D-bearing species long-used to detect deuterium in the solar system, deuterated water (HDO) and deuterated methane (CH_3D), on the spectra of free-floating planets and brown dwarfs. We consider objects below the deuterium-burning limit ($M < 13$ M_J). We include cloud-free objects with effective temperatures from 200 to 1800 K and log $g = 4.0$. These T_{eff}/g pairs cover a broad range of self-luminous free-floating planets. A 4.5 M_J planet will have a log $g = 4.0$ and $T_{eff} = 200$ K at $\sim$5 Gyr; a 10 M_J planet will have a log $g = 4.0$ and $T_{eff} = 1800$ K at $\sim$10 Myr. Radii range from 1.1 R_J (200 K) to 1.2 R_J (800 K) to 1.6 R_J (1800 K). Free-floating planets have been discovered throughout this temperature range (e.g., Cushing et al. 2011; Faherty et al. 2016). The surface gravity has little effect on the strength of the signal for the small range of surface gravities for objects with $M < 13$ M_J, so we use a single representative surface gravity.

Briefly, we calculate temperature structures assuming radiative–convective equilibrium as described in McKay et al. (1989), Marley et al. (1996, 1999), Saumon & Marley (2008), and Morley et al. (2012, 2014). The opacity database for gases is described in Freedman et al. (2014). The abundances of molecular, atomic, and ionic species are calculated using a modified version of the NASA CEA Gibbs minimization code (McBride & Gordon 1992). We include
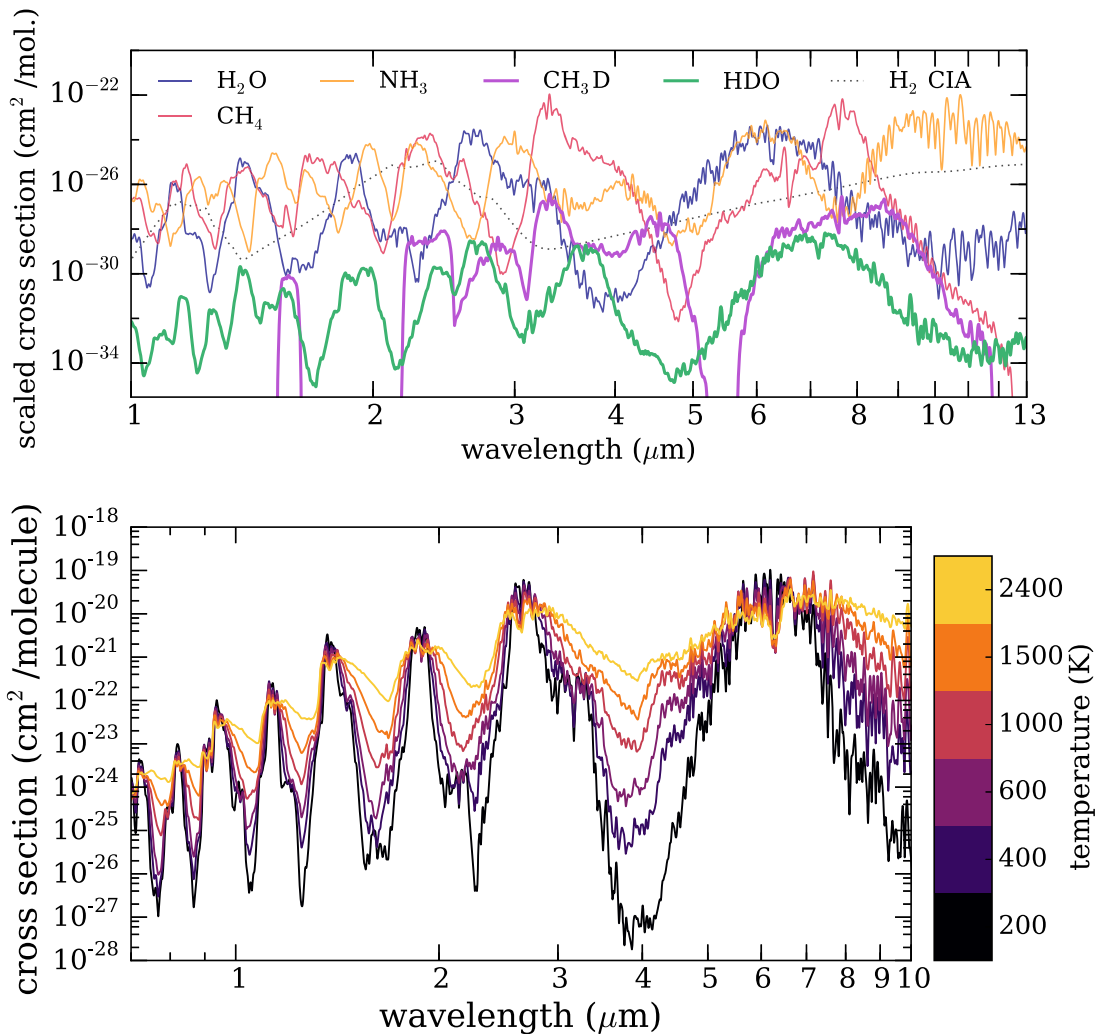
Figure 2. Molecular opacity cross sections for various species. The top panel shows cross sections for molecules important in cold brown dwarf atmospheres ($T = 225$ K, $P = 1$ bar). Cross sections are scaled by the abundance in chemical equilibrium, assuming D/H $= 2 \times 10^{-5}$. The bottom panel shows the cross section of H_2O at $P = 1$ bar and temperatures from 200 to 2400 K. Colder temperatures lead to larger amplitudes in molecular opacity.

condensation of cloud species to remove materials from the gas phase, including water and HDO at cold temperatures. Descriptions of recent updates to opacities and chemical equilibrium are described in M. S. Marley et al. (2019, in preparation).

We calculate moderate-resolution spectra using these pressure–temperature and abundance profiles with the Morley et al. (2015) thermal emission code, which uses the open-source radiative transfer code disort (Stamnes et al. 1988), which calculates intensities and fluxes in multiple-scattering and emitting layered media using the discrete-ordinate method.

We include HDO and CH_3D opacity when calculating moderate-resolution spectra. Cross sections are calculated using line lists from HITRAN 2012 for CH_3D (Rothman et al. 2013) and ExoMol for HDO (Janca et al. 2003; Voronin et al. 2010) and are shown in Figure 2. Our canonical cases assume a protosolar D/H ratio of 2×10^{-5}, typical for formation conditions of stars in the Local Group; CH_3D/CH_4 is taken to be $4 \times$ D/H in all our simulations and HDO/H_2O is $2 \times$ D/H, the factors arising from the multiple H atoms in each methane and water molecule.

One of the strongest molecular features of CH_3D is at $\sim$4.55 μm. This wavelength region is a "window" in

atmospheric opacity for cold brown dwarfs, since the important absorbers in the atmosphere—H_2O, CH_4, and NH_3—have low opacity at these wavelengths. For a trace species like CH_3D, a smaller amount of the species is necessary for it to be spectroscopically detectable at these window wavelengths because the path length through the atmosphere is longer. In contrast, HDO has features across the near- and mid-infrared (e.g., 3.7 μm), but these overlap with absorption features from the more abundant species.

4. Results

4.1. CH$_3$D is More Observable than HDO

Examples of our model spectra are shown in Figure 3, for a model with $T_{\text{eff}} = 250$ K and surface gravity of 4.0, representing a 4–5 M_J object with an age of 2 Gyr. Here we show the regions with the strongest CH_3D and HDO signals, respectively, for the temperature with the largest-amplitude HDO feature. We find that CH_3D has a substantially stronger impact on the spectrum than HDO; this is true at all temperatures studied here.

To quantify the observability of CH_3D and HDO, we simulate the G395H/F290LP grating/filter combination mode
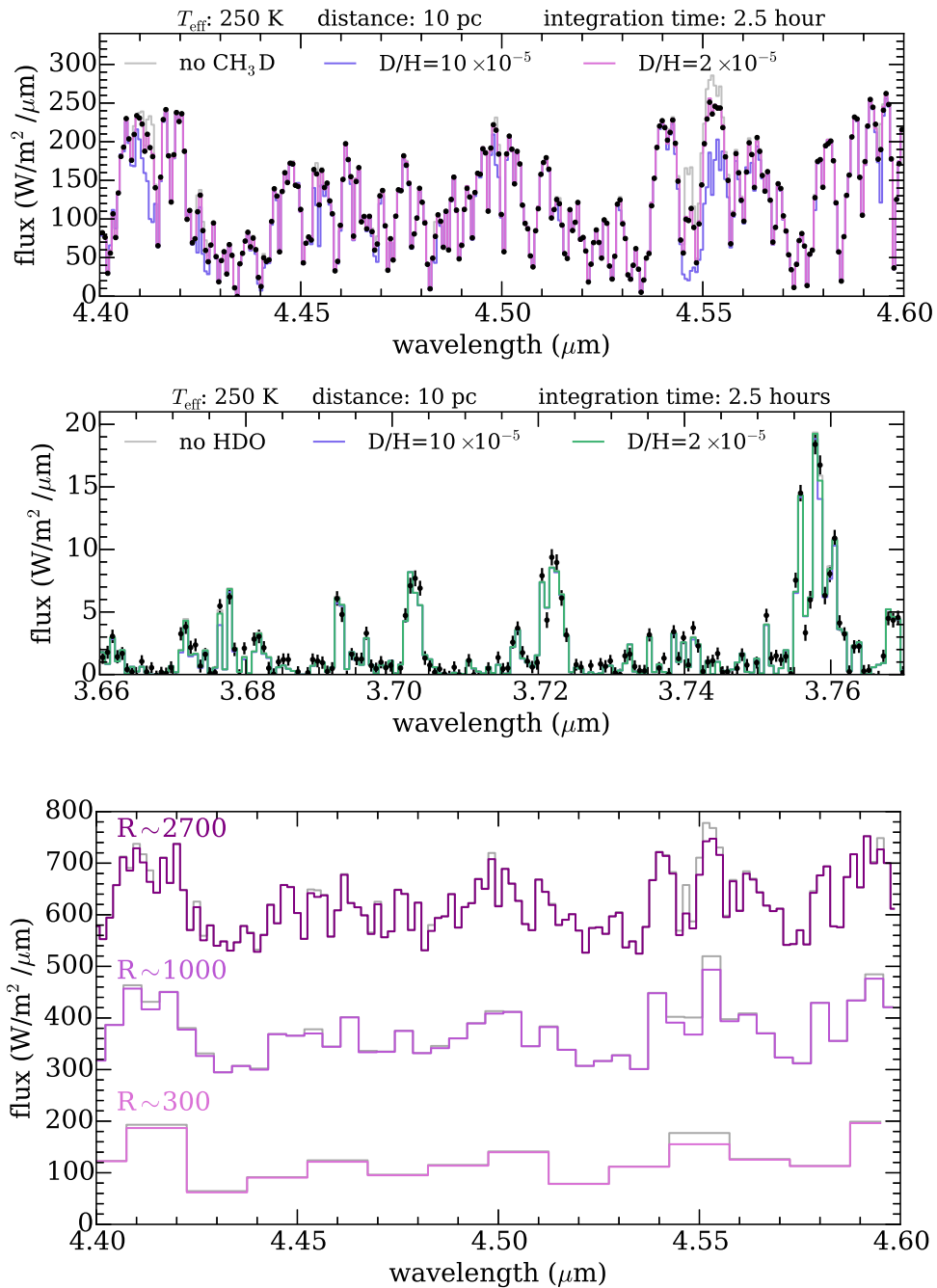
Figure 3. Model spectra and simulations of *JWST* data. The top and middle panels show model spectra (R~2700) including CH$_3$D and HDO, respectively, for a 250 K object (4–5 M_J, 2 Gyr). Model spectra include no D, protosolar D/H (2×10^{-5}), and 5× enhanced D/H (10×10^{-5}). Simulated data for a 2.5 hr observation (assuming a distance of 10 pc) with *JWST* are shown as black points with error bars. The bottom panel shows how changing spectral resolution changes the CH$_3$D feature for $R \sim 2700$, $R \sim 1000$, and $R \sim 300$.

of *James Webb Space Telescope* (*JWST*)/NIRSpec (2.87–5.14 μm, $R \sim 2700$), using the *JWST* online exposure time calculator tool (Pontoppidan et al. 2016). We assume that each object is 10 pc away, to match the distances of known cold brown dwarfs (of the known Y dwarfs, 14 of those with measured distances are within 11 pc and 8 more are within 20 (Leggett et al. 2017)). We assume total observation times of 2.5 hr, including dither time. Dithering is necessary because

above a signal-to-noise ratio (S/N) ~ 300, *JWST* is flat-field limited.[10]

While the 4.55 μm band of CH$_3$D is in one of the brightest wavelength regions for a cold brown dwarf, the 3.7 μm HDO band is within an absorption feature, so the brown dwarf is intrinsically fainter at those wavelengths. Spectra of cool brown dwarfs can therefore be measured at substantially higher S/N at 4.55 μm than 3.7 μm. Both the relative size of spectral features

---

and the underlying spectrum of the brown dwarf contribute to making CH$_3$D much easier to detect.

4.2. Minimum Resolving Power and Wavelength Ranges Needed

The molecular bands of CH$_3$D are relatively broad in wavelength (see Figure 2); however, to identify individual features within that broad band, a resolving power of ∼1000 is required (see the bottom panel of Figure 3). The most useful wavelength range is from 4 to 5 μm; CH$_3$D also has a feature at 8.5 μm, but with a higher background and fainter source at longer wavelengths with JWST/MIRI, the 4–5 μm region is always favored.

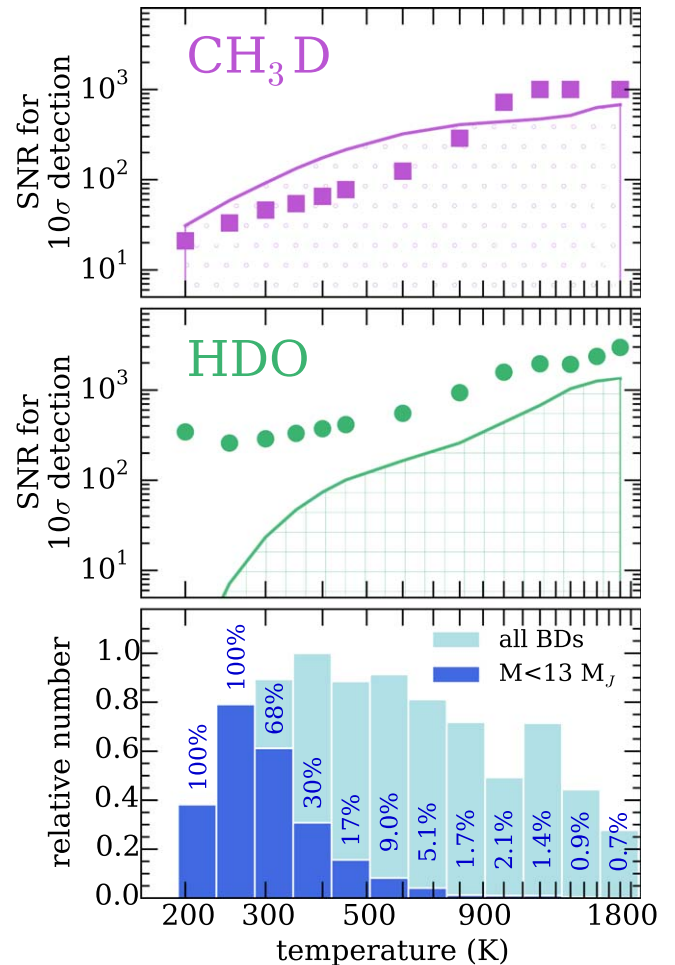### 4.3. Spectrum Signal-to-noise for D Detection

We calculate the signal to noise of the spectrum necessary to distinguish between a model with and without each deuterated species assuming a protosolar abundance (CH$_3$D/CH$_4$ = 4 × D/H = 8 × 10^{-5}; HDO/H$_2$O = 2 × D/H = 4 × 10^{-5}), using a chi-squared rejection test (Gregory 2005). We note that this is an imperfect method for claiming a "detection," but remains an intuitive way for the reader to picture the relative ease of detection for different simulated spectra. We verify this approach against a full Bayesian retrieval in Section 4.6.

The S/N needed generally increases with increasing temperature. HDO always requires an S/N greater than 200 for a 10σ detection; CH$_3$D requires an S/N less than 200 for objects with temperatures ≤600 K. Water and HDO condensation at $T_{\rm eff}$ < 400 K decrease the strength of HDO absorption for the coldest models.

Figure 4 summarizes our results; in the top two panels, the shaded regions show the S/N achievable in 2.5 hr, and the symbols show the S/N required for a 10σ nominal detection of the deuterated species. We find that HDO is never detectable in our simulated observations in a 2.5 hr integration. CH$_3$D is detectable in objects between 200 and 800 K in <2.5 hr. The bottom panel shows the fraction of brown dwarfs expected to be less massive than the 13 M_J deuterium-burning limit based on a simulated population; cold brown dwarfs are likely to be low mass and present the best targets for deuterium searches.

4.4. Temperature Strongly Controls Presence of D Features

Figure 4 clearly shows that $T_{\rm eff}$ strongly affects the strength of both CH$_3$D and HDO features; low-temperature objects require lower-S/N spectra. This is due to an intrinsic property of molecular opacities: the peak-to-trough amplitude of molecular cross sections in the infrared is strongly correlated with temperature; this is shown for water vapor in Figure 2 (bottom panel). At 200 K, the water cross section between 2.5 and 4.5 μm varies between ∼10^{-19} and 10^{-27} cm^2/molecule, while at 2000 K it varies between ∼10^{-20} and 10^{-22} cm^2/molecule. This striking difference—eight versus two orders of magnitude difference between the absorption band and window—means that the window regions of cold objects probe relatively deeper layers. The larger column of material probed means that a feature from a trace species like CH$_3$D is more prominent in a colder object. This fact has been exploited for decades to detect trace species at ∼5 μm in Jupiter, including CH$_3$D, PH$_3$, and GeH$_4$ (Bjoraker et al. 1986).


Figure 4. Detectability of deuterated species vs. temperature. The top and middle panels show the signal to noise needed for a 10σ detection of CH$_3$D and HDO, respectively, assuming a spectrum from 3 to 5 μm with $R \sim 2700$. The hatched regions show the S/N predicted per spectral element in the region of the spectrum with CH$_3$D or HDO features in a 2.5 hr observation with JWST. CH$_3$D is detectable at high significance for objects cooler than 800 K; HDO is never detectable at high significance in 2.5 hr. The bottom panel shows a simulated brown dwarf population from Saumon & Marley (2008); it uses a power-law initial mass function (IMF) index $\alpha = 1$, masses between 0.006 and 0.1 $M_{\rm Sun}$, and uniform age distribution between 0 and 10 Gyr.

4.5. Effect of Enhanced Atmospheric Metallicity and D/H Ratio

The atmospheres of extrasolar Saturns and Neptunes may be significantly enhanced in metals. We simulate additional spectra with $T_{\rm eff}$ = 320 K, chosen to represent a young super-Neptune to Saturn-mass object (30–100 $M_{\rm Earth}$) at 1–20 Myr. We aim to determine how the detectability of CH$_3$D scales with metal enhancement, using Jupiter-like (3 × solar), Saturn-like (10 × solar), and Neptune-like (100 × solar) metallicities and D/H ratios of 2×10^{-5} (protosolar) and 5×10^{-5} (Neptune-like). An example spectrum with high metallicity and enhanced D/H is shown in Figure 5.

The strength of the CH$_3$D feature scales with metallicity; increasing the metal enhancement by a factor of 10 decreases the signal to noise needed by a factor of ∼3. Similarly, increasing the D/H ratio decreases the S/N needed. These results are summarized in the center panel of Figure 5.

The temperature evolution of Neptune- and Saturn-mass objects is shown in Figure 5, calculated using the
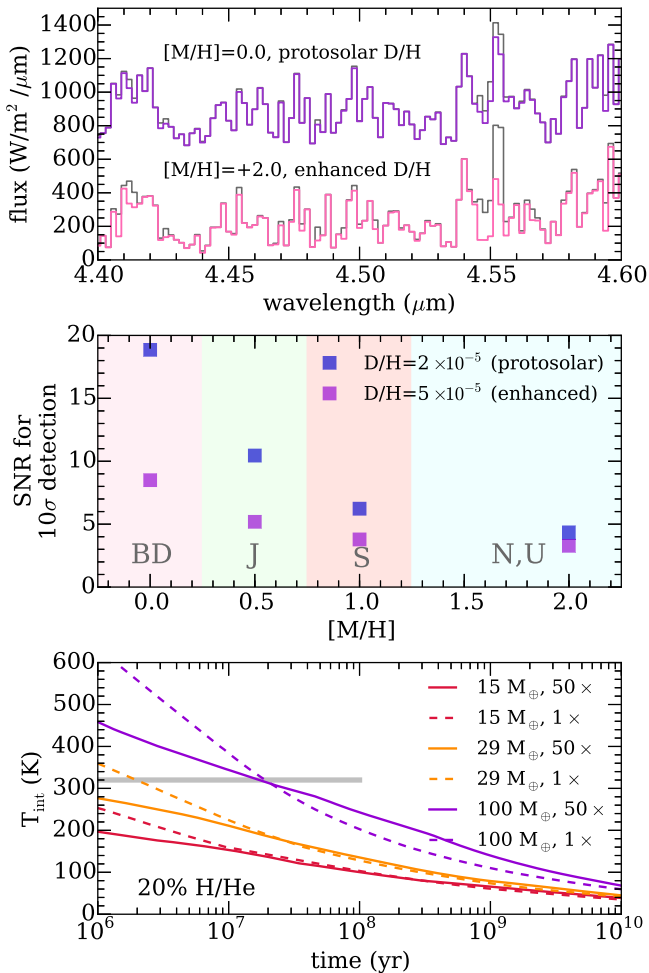
Figure 5. Top panel: model spectra, offset for clarity, of a 320 K, $g = 15\,\mathrm{m\,s^{-2}}$, cloud-free object; top model is solar metallicity, with no CH_3D (gray line) and a protosolar (2×10^{-5}) D/H ratio (purple line); bottom model is $100\times$ solar metallicity with no CH_3D (gray line) and enhanced (5×10^{-5}) D/H ratio (pink line). Middle panel: S/N per spectral element needed to detect CH_3D as a function of metallicity for protosolar and enhanced D/H ratios for a planet with $T = 320$ K, $g = 15\,\mathrm{m\,s^{-2}}$. CH_3D is easier to detect in high-metallicity objects and for enhanced D/H ratios. Regions are shaded according to the metallicities of local brown dwarfs and solar system giant planets. Bottom panel: intrinsic temperatures of model planets over time for solar and $50\times$ solar metallicity atmospheric boundary conditions, assuming a 20% H/He planet by mass. The 320 K temperature modeled above corresponds to a 20 Myr Saturn-mass planet or a 1–2 Myr super-Neptune.

methodologies described in Lopez & Fortney (2014), assuming that Neptunes have high initial entropies ("hot start") and cloud-free atmospheres. Young (10 Myr old) Saturn-mass objects are predicted to have temperatures around 400 K and cool to $\sim$200 K within 100–300 Myr. Neptune-mass planets are colder, with temperatures around 250 K at 10 Myr. Planets in this mass range may be detectable with *JWST* (Beichman et al. 2010; Schlieder et al. 2016).

4.6. Retrieving D/H Ratios from JWST Spectra

Using the atmospheric retrieval tools recently applied to brown dwarfs (Line et al. 2015, 2017) we quantitatively determine the degree to which we can constrain the CH_3D/CH_4 ratio with NIRSpec on *JWST* assuming that our models perfectly represent real cold brown dwarfs. We use the identical forward model parameterization and Bayesian parameter

estimation tools to those presented in Line et al. (2015, 2017), but the model is upgraded to include PH_3 and CH_3D. We tailor the retrieval setup to match the atmospheric structure of a 300 K, $\log g = 5$ (cgs), solar metallicity, cloud-free Y dwarf with $D/H = 2 \times 10^{-5}$. We freely fit the abundances of each species individually, pressure–temperature profile, surface gravity, temperature, and radius.

We find that we can constrain the ratio of CH_3D/CH_4 to $(8.0 \pm 0.2) \times 10^{-5}$ with a 2.5 hr observation, assuming the same noise models as in Section 4.1, corresponding to a D/H ratio of $(2.0 \pm 0.05) \times 10^{-5}$. These constraints are remarkable, but in these simulations the forward model is a perfect match to the data; hidden, unforeseen assumptions, or systematic errors will inhibit these constraints.

5. Discussion

5.1. Converting CH3D/CH4 to D/H

Above, we assumed CH_3D/CH_4 equals $4 \times D/H$ (i.e., the molecules are in isotopic equilibrium). However, isotopic exchange depends on temperature. Deep, hotter layers are expected to be in isotopic balance, but colder upper layers probed by these measurements may not be. The actual CH_3D/CH_4 ratio is determined by a vertical mixing timescale and isotopic exchange timescale. At the top of the atmosphere, the relative abundance f of CH_3D/CH_4 compared to bulk D/H is 1.25 for Jupiter, 1.38 for Saturn, 1.68 for Uranus, and 1.61 for Neptune (Lecluse et al. 1996). The objects considered here are hotter than these planets, and would therefore be closer to isotopic balance ($f = 1.0$–1.25). Our approximation is conservative; if f is higher, the amount of CH_3D is larger and therefore easier to detect.

5.2. Clouds

Cloud opacity is not included in these calculations. Clouds typically mute features in thermal emission spectra, so if objects of interest are extensively cloudy, these species would be harder to observe. Brown dwarfs with $T_{\mathrm{eff}} > 1200$ K have extensive refractory clouds (silicates/iron), while colder objects are relatively well matched by cloud-free models (e.g., Cushing et al. 2008) until water clouds form for objects less than 375 K (Morley et al. 2014). Using cold models with thick water ice clouds, we find that cloud-free simulations underestimate the S/N needed to detect CH_3D features by $\sim$40%–50%.

5.3. Interior Physics, Masses, and Ages of the Coldest Brown Dwarfs

For objects with known masses, detecting deuterium could allow us to estimate their ages and test models of deuterium fusion as a function of mass. Our calculations demonstrate that deuterium is most observable in the coldest brown dwarfs, the Y dwarfs. The bottom panel of Figure 4 shows a simulation of the number of brown dwarfs at a given temperature, assuming that the initial mass function is a power law (index $\alpha = 1$), and with a uniform age distribution between 0 and 10 Gyr (Saumon & Marley 2008). A 13 M_J object cools to 300 K in 10 Gyr, so for objects under $\sim$300 K, all simulated objects have masses less than the deuterium-burning limit ($M < 13M_J$). For objects between 300 and 400 K, $\sim$30%–68% have $M < 13M_J$; for hotter objects, the fraction of brown dwarfs with $M < 13M_J$

drops off to ∼1%–2% for $T_{eff} > 800$ K (Saumon et al. 1996; Spiegel et al. 2011).

Quantifying the presence of deuterium in a range of Y dwarf atmospheres tests the assumptions made in the simulation and thus the properties of field brown dwarfs. Recent work by Dupuy & Liu (2017) showed that nearby brown dwarfs with mass measurements have systematically younger ages (a median of 1.3 Gyr and an age interval of 0.4–4.2 Gyr for a sample of 10 systems) than the 0–10 Gyr range simulated here; thus, more of them are likely to be deuterium-rich. Sampling a range of 250–500 K objects would test this prediction and provide an independent way of measuring the age of local substellar objects.

5.4. Detecting Deuterium with High-dispersion Spectroscopy from Ground-based Telescopes

Mollière & Snellen (2019) recently showed that deuterium may be detectable for exoplanets from the ground using high-dispersion spectroscopy. They find that CH_3D may be detectable at 4.7 μm using current instruments for transiting planets below 700 K. Future ELT-class telescopes will allow detections for a wide range of planets. They also find that HDO is more challenging because methane shields HDO absorption. This technique will be complementary to the moderate-resolution spectroscopy with telescopes like *JWST* considered here.

5.5. Planet Formation and Envelope Accretion

In our own solar system, the two largest giant planets, Jupiter and Saturn, have D/H abundances consistent with the protosolar nebula, while the lower-mass Neptune and Uranus are enhanced by a factor of several due to accretion of ices during planet formation. Measuring deuterium enhancement or depletion in exoplanets allows us to test planet formation mechanisms in other systems. Multiplanet systems will be particularly valuable since the primordial D/H ratio varies within the galaxy.

JWST will be capable of detecting cool Jupiters and Neptunes around nearby M dwarfs (Beichman et al. 2010; Schlieder et al. 2016). Jupiter-mass exoplanets with ages of 100–300 Myr will have temperatures of 250–300 K (Fortney et al. 2008) and radii of 1.1–1.15 R_J, so if any such nearby planets are discovered with *JWST*, they will require comparable S/N spectra to the free-floating objects considered here to detect CH_3D.

Young objects (10 Myr) with masses twice that of Neptune are predicted to have temperatures around 200–225 K and radii around 6–9 R_{Earth}. If their atmospheres are enhanced in metals and in deuterium, CH_3D may be detectable in their spectra (see Section 4.5).

6. Conclusions

In this Letter, we have presented spectra of model brown dwarfs and free-floating planets including both HDO and CH_3D for objects from 200 to 1800 K. CH_3D requires a lower-S/N spectrum to detect than HDO at all temperatures. Colder objects have stronger spectral features due to the inherent properties of the cross sections of molecular species, which have larger differences in absorption between troughs and peaks at colder temperatures. For objects from 200 to 800 K, a protosolar D/H ratio of 2×10^{-5} would be detectable in

spectra with average S/N per spectral element between 20 and 100, readily achievable for these objects with 2.5 hr of integration time with *JWST*, assuming a typical distance of 10 pc. Colder objects will have stronger lines, but require more time to observe since they are fainter; warmer objects have weaker lines that are not readily observable with *JWST*.

The D/H ratio has been an important tracer of planet formation, gas accretion, and atmosphere evolution in the solar system since the 1970s when CH_3D was first detected in Jupiter. For brown dwarfs and free-floating planets in the near future, similar measurements will allow us to map their masses and ages and test models of their interior physics. For exoplanets from Neptune to Jupiter mass, D/H measurements will allow us to understand envelope accretion for planets outside the solar system. These measurements pave the way for future studies of terrestrial planets, for which D/H measurements trace the accretion of their atmospheres and their evolution over their lifetimes.

ORCID iDs

Caroline V. Morley ⓘ https://orcid.org/0000-0002-4404-0456
Andrew J. Skemer ⓘ https://orcid.org/0000-0001-6098-3924
Brittany E. Miles ⓘ https://orcid.org/0000-0002-5500-4602
Michael R. Line ⓘ https://orcid.org/0000-0002-2338-476X
Matteo Brogi ⓘ https://orcid.org/0000-0002-7704-0153
Mark S. Marley ⓘ https://orcid.org/0000-0002-5251-2943

References

Beer, R., Farmer, C. B., Norton, R. H., Martonchik, J. V., & Barnes, T. G. 1972, Sci, 175, 1360
Beichman, C. A., Krist, J., Trauger, J. T., et al. 2010, PASP, 122, 162
Bjoraker, G. L., Larson, H. P., & Kunde, V. G. 1986, Icar, 66, 579
Chamberlain, J. W., & Hunten, D. M. 1987, Theory of Planetary Atmospheres. An Introduction to Their Physics and Chemistry (Orlando, FL: Academic Press Inc.), 368
Charbonneau, D., Brown, T. M., Noyes, R. W., & Gilliland, R. L. 2002, ApJ, 568, 377
Cleeves, L. I., Bergin, E. A., Alexander, C. M. O., et al. 2014, Sci, 345, 1590
Courtin, R., Gautier, D., Marten, A., Bezard, B., & Hanel, R. 1984, ApJ, 287, 899
Cushing, M. C., Kirkpatrick, J. D., Gelino, C. R., et al. 2011, ApJ, 743, 50
Cushing, M. C., Marley, M. S., Saumon, D., et al. 2008, ApJ, 678, 1372
de Bergh, C., Lutz, B. L., Owen, T., Brault, J., & Chauville, J. 1986, ApJ, 311, 501
de Bergh, C., Lutz, B. L., Owen, T., & Maillard, J.-P. 1990, ApJ, 355, 661
Donahue, T. M., & Pollack, J. B. 1983, in Venus, ed. D. M. Hunten et al. (Tucson, AZ: Univ. Arizona Press), 1003
Drake, M. J. 2005, M&PS, 40, 519
Drake, M. J., & Righter, K. 2002, Natur, 416, 39
Dupuy, T. J., & Liu, M. C. 2017, ApJS, 231, 15
Espinoza, N., Fortney, J. J., Miguel, Y., Thorngren, D., & Murray-Clay, R. 2017, ApJL, 838, L9
Faherty, J. K., Riedel, A. R., Cruz, K. L., et al. 2016, ApJS, 225, 10
Feuchtgruber, H., Lellouch, E., Bézard, B., et al. 1999, A&A, 341, L17

Fortney, J. J., Marley, M. S., Saumon, D., & Lodders, K. 2008, ApJ, 683, 1104

Freedman, R. S., Lustig-Yaeger, J., Fortney, J. J., et al. 2014, ApJS, 214, 25

Gregory, P. C. 2005, Bayesian Logical Data Analysis for the Physical Sciences: A Comparative Approach with "Mathematica" Support (Cambridge: Cambridge Univ. Press)

Guillot, T. 1999, P&SS, 47, 1183

Hartogh, P., Lis, D. C., Bockelée-Morvan, D., et al. 2011, Natur, 478, 218

Janca, A., Tereszchuk, K., Bernath, P., et al. 2003, JMoSp, 219, 132

Kirkpatrick, J. D. 2005, ARA&A, 43, 195

Knacke, R. F., Kim, S. J., Ridgway, S. T., & Tokunaga, A. T. 1982, ApJ, 262, 388

Kreidberg, L., Bean, J. L., Désert, J.-M., et al. 2014, ApJL, 793, L27

Kunde, V., Hanel, R., Maguire, W., et al. 1982, ApJ, 263, 443

Lecluse, C., Robert, F., Gautier, D., & Guiraud, M. 1996, P&SS, 44, 1579

Leggett, S. K., Tremblin, P., Esplin, T. L., Luhman, K. L., & Morley, C. V. 2017, ApJ, 842, 118

Lellouch, E., Bézard, B., Fouchet, T., et al. 2001, A&A, 370, 610

Lellouch, E., Hartogh, P., Feuchtgruber, H., et al. 2010, A&A, 518, L152

Line, M. R., Marley, M. S., Liu, M. C., et al. 2017, ApJ, 848, 83

Line, M. R., Teske, J., Burningham, B., Fortney, J. J., & Marley, M. S. 2015, ApJ, 807, 183

Lopez, E. D., & Fortney, J. J. 2014, ApJ, 792, 1

Marley, M. S., Gelino, C., Stephens, D., Lunine, J. I., & Freedman, R. 1999, ApJ, 513, 879

Marley, M. S., Saumon, D., Guillot, T., et al. 1996, Sci, 272, 1919

McBride, B. J., & Gordon, S. 1992, NASRP, 92 https://www.grc.nasa.gov/www/CEAWeb/RP-1271.htm

McKay, C. P., Pollack, J. B., & Courtin, R. 1989, Icar, 80, 23

Mollière, P., & Snellen, I. A. G. 2019, A&A, 622, A139

Morley, C. V., Fortney, J. J., Marley, M. S., et al. 2012, ApJ, 756, 172

Morley, C. V., Fortney, J. J., Marley, M. S., et al. 2015, ApJ, 815, 110

Morley, C. V., Marley, M. S., Fortney, J. J., et al. 2014, ApJ, 787, 78

Öberg, K. I., Murray-Clay, R., & Bergin, E. A. 2011, ApJL, 743, L16

Owen, T. 1992, in IAU Symp. 150, Astrochemistry of Cosmic Phenomena, ed. P. D. Singh (Dordrecht: Springer), 97

Pettini, M., Zych, B. J., Murphy, M. T., Lewis, A., & Steidel, C. C. 2008, MNRAS, 391, 1499

Pierel, J. D. R., Nixon, C. A., Lellouch, E., et al. 2017, AJ, 154, 178

Pontoppidan, K. M., Pickering, T. E., Laidler, V. G., et al. 2016, Proc. SPIE, 9910, 991016

Prodanović, T., Steigman, G., & Fields, B. D. 2010, MNRAS, 406, 1108

Rothman, L. S., Gordon, I. E., Babikov, Y., et al. 2013, JQSRT, 130, 4

Saumon, D., Hubbard, W. B., Burrows, A., et al. 1996, ApJ, 460, 993

Saumon, D., & Marley, M. S. 2008, ApJ, 689, 1327

Schlieder, J. E., Beichman, C. A., Meyer, M. R., & Greene, T. 2016, in IAU Symp. 314, Young Stars and Planets Near the Sun, ed. J. H. Kastner, B. Stelzer, & S. A. Metchev (Cambridge: Cambridge Univ. Press), 288

Spiegel, D. S., Burrows, A., & Milsom, J. A. 2011, ApJ, 727, 57

Stamnes, K., Tsay, S.-C., Jayaweera, K., & Wiscombe, W. 1988, ApOpt, 27, 2502

Stevenson, D. J. 1982, P&SS, 30, 755

Voronin, B. A., Tennyson, J., Tolchenov, R. N., Lugovskoy, A. A., & Yurchenko, S. N. 2010, MNRAS, 402, 492